AIAA JOURNAL
Vol. 40, No. 11, November 2002

Nonisotropic Model of Microdebris from Impacts with Complex Targets

Gregory R. Kruse*
Computer Sciences Corporation, Huntsville, Alabama 35815
and
William P. Schonberg†
University of Missouri–Rolla, Rolla, Missouri 65409

Microdebris particles generated by hypervelocity impacts between complex projectiles and ballistic missile targets can affect sensitive components of such aerospace systems. Current models assume an isotropic dispersion of this microdebris about the postimpact debris cloud center of mass. Data collected from recent tests indicate that a nonisotropic microdebris dispersion model is needed. The results are presented of a study aimed at improving the capabilities of an existing model that characterizes the microdebris environment created in a high-speed impact. Following a review of test data collection techniques, a nonisotropic microdebris dispersion model is developed as a series of modifications to the existing microdebris size distribution model. Relevant test data are then used to evaluate the proposed nonisotropic model. It is found that the modified model is more correct in accounting for the microdebris fragment population created in a high-speed impact than the current isotropic dispersion model.

Nomenclature

A_{surface}	=	surface area of a sphere
a	=	point on shotline located a vertical distance (parallel to X'') and horizontal distance (parallel to Y'') from target c.g.
b	=	point where projectile path intersects exterior surface of target
C	=	distance from target nose to target c.g.
D	=	target diameter
L	=	target overall length
N	=	number of fragments exceeding a given fragment size
P	=	arbitrary point
R	=	range from target c.g. to collection device
r	=	radius of sphere
r_p	=	distance from origin to point P in target coordinate Y–Z plane
r'_p	=	distance from origin to arbitrary point P in temporary target coordinate system X–Z plane
X, Y, Z	=	X, Y, and Z axes in target coordinate system
X_p, Y_p, Z_p	=	X, Y, and Z coordinate of point P
X', Y', Z'	=	X, Y, and Z axes in temporary target coordinate system
X'_p, Y'_p, Z'_p	=	X', Y', and Z' coordinate of point P
X'', Y'', Z''	=	X, Y, and Z axes in test chamber coordinate system
X''_p, Y''_p, Z''_p	=	X'', Y'', and Z'' coordinate of point P
α	=	elevation angle between microdebris bias vector and witness panel, deg
β	=	angle between line segment from origin to point P and target coordinate Y axis
β'	=	angle between line segment from origin to point P and temporary target coordinate system Z' axis
γ	=	coefficient in beta distribution function
θ	=	horizontal angle from shotline to collection device, deg
λ	=	coefficient in beta distribution function
ϕ	=	vertical angle from shotline to microdebris collector, deg

Received 14 January 2000; revision received 20 July 2001; accepted for publication 19 June 2002.

*Staff Engineer, 4090 South Memorial Parkway.
†Professor and Chair, Civil Engineering Department. Associate Fellow AIAA.

Introduction

HYPERVELOCITY impacts associated with ballistic missile defense intercepts can produce tens of billions of fragments in excess of several micrometers in size. Whereas micrometer-sized fragments, that is, microdebris, are unlikely to result in structural damage in subsequent encounters with aerospace systems, they are capable of affecting sensitive components associated with these systems. Such components include optical sensors, solar cell arrays, and communication antennas. As a result, there is a need to be able to quantify accurately the microdebris environments associated with hypervelocity impacts and to develop simulations that model and propagate these environments.

The kinetic impact debris distribution (KIDD) simulation[1] is a semi-empirical Monte Carlo code based on data collected from a wide range of flight tests, light-gas gun tests, and rocket sled tests representing a variety of projectiles, targets, velocities, and geometries. These data have been used to develop a series of models for debris fragment sizes, shapes, areas, materials, masses, velocities, temperatures, and ballistic coefficients.[2] A database representing over 43,000 fragments exceeding 1 mm in size has been used to develop and validate these models. Recent efforts, including the work presented in this paper, have emphasized obtaining data and refining the models in KIDD for debris sizes extending down to 1 μm.

The current version of KIDD makes the simplifying assumption that microdebris expands isotropically from both the projectile and target debris cloud postimpact centers of mass. However, examination of data collected from recent tests has revealed that the geometry of impact and target/projectile characteristics are expected to result in biased, nonisotropic microdebris expansions. As a result, new techniques are needed to support improved KIDD models for expanding microdebris clouds. This paper presents the results of efforts aimed at reducing the amount of extrapolation at small fragment sizes and better characterizing microdebris direction and size distributions. For the purpose of the study described herein, microdebris are defined as debris fragments smaller than 100 μm in size. This size threshold is used because very few microdebris impacts larger than 100 μm were observed during test data analysis.

Following a discussion of the methods and assumptions used to reduce test data, efforts to improve the KIDD microdebris model are presented and discussed. These efforts include the development of a dispersion direction microdebris bias vector (MBV) and modifications to the KIDD small fragment size distribution slopes. Finally, predictions of the modified microdebris model are compared to actual test data.

Test Data Reduction

Introduction

Ideally, a model defining the microdebris environment immediately following an impact between a complex projectile and ballistic missile target would predict microdebris direction, velocity, and temperature (material phase). Because dedicated tests with sufficient instrumentation to measure fully these environments were not possible, microdebris data collection efforts were conducted as noninterfering piggyback experiments conducted during high-speed impact tests against complex, multimaterial, multilayered targets. As a result, the number and/or location of collection devices were not always optimal. In this section, we discuss the difficulties associated with data collection in this type of environment and some of the assumptions made to account for test chamber effects. We also review available test data[3,4] and highlight data that apply to the objective of understanding nonisotropic microdebris dispersion.

Data Collection

Different types of collection media were used to obtain information about microdebris clouds resulting from hypervelocity impacts between complex vehicles. Instrumentation included fragment spin velocimeters,[3,4] which utilized a rotating witness panel positioned behind fixed apertures; makescreens, which were used to determine the leading-edge velocity of the debris cloud; and static witness panels of various materials and thicknesses, which were used to record the microdebris deposition at multiple locations in the impact chamber. A review of the available test data[3,4] reveals them to be rather sparse in some instances, less so in others, and occasionally fairly complete. This variation in the completeness of the data is primarily because the microdebris collection devices were added wherever space permitted within the test camber.

The piggyback nature of data collection prevented the ideal number and placement of microdebris witness panels (or fragment velocimeters). Another contributor to sparse witness panel data in some of the tests is posttest recovery. Witness panels were attached to bundles of soft-catch material that surrounded the impact area. During each test, large debris fragments pulverized this soft-catch material. Approximately 5.7 m^3 of this soft-catch, large debris fragment and witness panel mix were shoveled into trash cans and then hand sifted to recover target debris and witness panels.[4]

The very nature of this type of hand sort, combined with the extremely harsh test chamber environment during impact, resulted in witness panel recovery as low as 50% on some tests and as high as 100% on others. On later tests where thicker witness panels were used, recovery was higher. Unfortunately, but not unexpectedly, some unrecovered panels were at locations receiving the most harsh microdebris environment. As a result, witness panel locations did not adequately cover the full 4π sr surrounding the target. In subsequent analyses, data from multiple tests are combined to provide sufficient data to observe the nonisotropic nature of the microdebris cloud.

Test Chamber Effects

There are indications that the microdebris can be at a molten or near molten state when it reaches the witness panel. It is uncertain at this time as to whether the microdebris is in this state immediately after impact or whether it is heated as it travels the 1–2 m in the test chamber to the witness panel by interacting with the chamber environment. Small debris particles traveling at speeds between 1 and 6 km/s in a low-pressure atmosphere result in low Reynolds numbers, causing high aerodynamic drag. A key factor in understanding this phenomenon is to understand free molecule flow conditions, where particle sizes are about the same as the mean free path between molecules in low-pressure air. The resulting particle-to-molecule collisions may result in the heating and deceleration of the smaller microdebris particles, that is, smaller than 10 μm, as they travel toward the witness panels. However, an analysis relating to free molecule flow is beyond the scope of this study, and the characterization of this effect is deferred to a later time.

Another light-gas gun test chamber effect that should be considered is the high-velocity gas following the projectile into the impact chamber at the time of impact. Most of this gas is contained uprange in blast tanks. High-speed cameras indicate, however, that some swirling gases do reach the impact area. Because of the delayed arrival time of this gas, and based on further review of the high-speed film, it is assumed that the microdebris has sufficient time to reach the witness panels before it is affected by this gas.

The possibility of microdebris ricochet off the chamber wall, which would increase the effective witness panel surface area by reflecting microdebris not originally dispersed in the witness panel's direction into the witness panel, was investigated. In one of the tests, a witness panel was installed facing away from the impact point. This sample was analyzed after the test, and no microdebris deposition was observed. It is assumed, therefore, that microdebris depositions considered in this study are the result of flight in a direct path from the impact point to the witness panel.

Data Reduction and Observations

Posttest Microdebris Identification and Measurement

Microdebris deposition materials were identified using scanning electron microscope/energy/dispersive x-ray (SEM/EDX) analyses. The SEM/EDX provides composition information for all elements that may be present, from boron through uranium. SEM/EDX analyses were only performed on witness panels that appeared to be able to yield useful microdebris material and deposition data. Highest priority was placed on witness panels that only received target microdebris deposition. Therefore, the ability to differentiate between target and projectile microdebris using the SEM/EDX is very important. Target and projectile materials as well as elements used in their alloys were carefully scrutinized.

Photomicrographs were taken of small witness panel areas so that microdebris size distributions could be measured. Various magnifications were used, depending on the amount of microdebris deposition on the witness panel. This was done to keep the number of microdebris impacts at a manageable level for manual size measurements. Low magnifications, that is, 80× were used for panels with light deposition. Higher magnifications, that is, 200× were used for heavy deposition. A typical 100× photomicrograph is shown in Fig. 1. This photomicrograph was taken with a SEM; similar

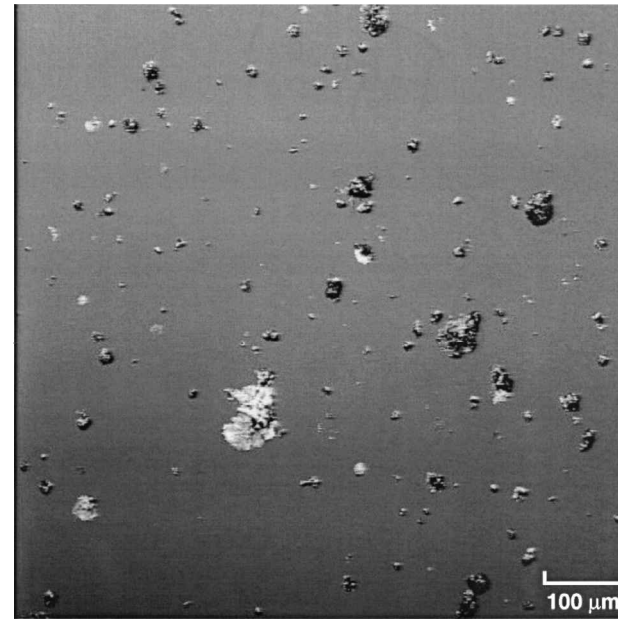

Fig. 1 Photomicrograph example.

photomicrographsused in subsequentanalyses were taken using an optical microscope.

Microdebris size distributions were generated by measuring the size of each microdebris impact from an enlarged witness panel photomicrograph.Enlargements were made to reduce measurement errors associated with small photographs. Because it is impossible to recover and measure the millions of microdebris fragments generated in an impact, a revised method of reporting the size distribution must be used. This is accomplished by normalizing the size distribution to the surface area of a sphere at a given radius as follows.

Consider the millions of microdebris fragments expanding radially in all directions from the impact point through the boundary of a sphere. For an isotropic expansion, that is, equal probability of dispersion in all directions, a normalized size distribution can be calculated using

$$\text{number/cm}^2 \text{ exceeding} = \text{number exceeding}/A_{\text{surface}} \quad (1)$$

where $A_{\text{surface}} = 4\pi r^2$ is the surface area of the sphere (with radius r). As such, this represents the number of fragments passing through a unit area of a sphere at radius r.

Two normalized size distributions at different ranges from the impact point (or sphere radii) can then be compared by simply modifying one normalized size distribution to the same sphere radius as follows:

$$\text{number/cm}^2 \text{ exceeding}_2 = \text{number/cm}^2 \text{ exceeding}_1 (r_1/r_2)^2 \quad (2)$$

where number/cm^2 exceeding$_1$ and r_1 are the number of fragments per square centimeter exceeding a given size and witness panel radius, respectively, from witness panel 1. Similarly, number/cm^2 exceeding$_2$ and r_2 are the number of fragments per square centimeter exceeding a given size and witness panel radius, respectively, from witness panel 2.

Microdebris sizes measured from a photomicrographon one witness panel can now be easily compared to other measured photomicrograph size distributions or model predictions using this surface area and range normalization technique. For example, suppose a 100× witness panel photomicrograph has a surface area of 0.016 cm^2 and was placed, before impact, at a range of 179 cm to the target c.g. Two steps are required to normalize this measured size distribution. First, measured cumulative fragment numbers are divided by the measured witness panel surface area using Eq. (1). ($A_{\text{surface}} = 0.016$ cm^2 in this case.) Second, the distribution is normalized to a 150 cm radius using Eq. (2), that is, it is multiplied by $(179/150)^2$.

Henceforth, all microdebris size distributions from witness panel measurements and model predictions will be normalized and scaled to a 150-cm range to facilitate comparisons between tests. For ease of readability, when shown the x axis will range from 1 to 100 μm (0.0001 to 0.01 cm) and the y axis will have a minimum value of 1. Although it will not be shown, note that subsequent demonstrated data still extend to meet the large fragment data.

Splatter Effects

When comparing microdebris deposition test data from witness panels to model predictions, the amount of growth each fragment experiences as it "splatters" onto the witness panel must be considered. This is accomplished by the use of error bars. Because KIDD predicts fragment size before it is deposited on the witness panel, the deposition size measured on each witness panel is given a negative error bar based on the estimated amount of growth. These error bars are estimated using a volumetric approach. Figure 2 shows an edge-on (80 deg from normal) SEM image of microdebris deposition at 1700×. The large black area in Fig. 2 is a dust particle. The length and height of the deposition to the right of that dust particle was measured, and its volume was calculated. A volume was equivalent sphere diameter was calculated to be one-half of the compared length of the measured deposition, indicating in a growth factor of 2, that is, growth factor equals deposition size divided by original fragment size.

Several deposits on other samples were also volumetrically analyzed. These deposits all had calculated growth factors between 2 and 3. A qualitative visual inspection of several SEM images, however, reveals that some deposits could have experienced growth as high as 4 or 5 times the size of the original particle diameter. Error bars with a growth factor of 5, therefore, will be used in the following analyses, with the understanding that most growth factors are more likely to be between 2 and 3.

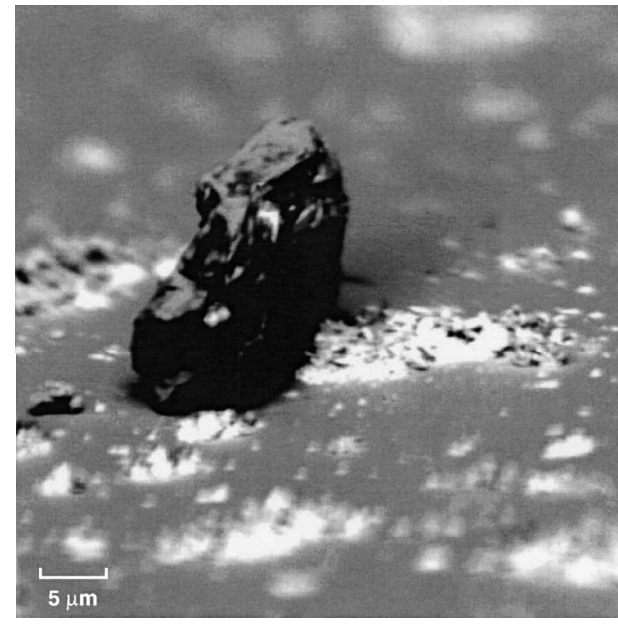

Fig. 2 Sample SEM image at 1700×.

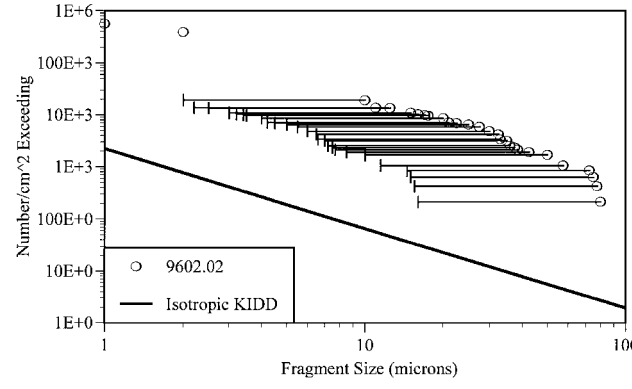

Fig. 3 Deposition measurement for sample 9602.02.

Comparison of Microdebris Data and KIDD Predictions

A series of 10 tests performed at the University of Alabama in Huntsville/Aerophysics Research Center (UAH/ARC) provides the best opportunity to measure microdebris density and dispersion direction. The hard polished surface of sapphire witness panels turned out to be excellent for microdebris collection and measurement. Other benefits of sapphire witness panels are their ease in mounting in the test chamber, posttest cleaning, and flat surface for SEM/EDX analyses.

Figure 3 shows a fragment size distribution plot that is typical of these 10 tests. As can be seen in Fig. 3, the isotropic KIDD size distribution underpredicts the number of microdebris fragments by more than an order of magnitude. When a 5× growth factor is assumed (shown using error bars in Fig. 3), KIDD still underpredicts the microdebris environment by an order of magnitude. Note that the test data shown are from witness panels that were mounted at various uprange and downrange test chamber locations, that is, various dispersion directions. These discrepancies between the existing KIDD model and test data are too large to model with the most nonisotropic of dispersion models. Efforts aimed at reducing these discrepancies are addressed in the next two sections.

Nonisotropic Microdebris Cloud Model

At the heart of the nonisotropic microdebris model developed herein is the MBV. The MBV is a vector that is defined using target dimensions and the impact geometry parameters used in light–gas gun tests as well as in KIDD. It also provides a reference direction based on a given impact condition, which can subsequently be used to define nonisotropic debris dispersion. This directional reference is necessary for a debris characterization model such as KIDD to be able to assign a direction to a postimpact fragment.

Geometry, coordinate systems, and methodology for calculating the MBV are introduced in this section. These geometries and coordinate system transformations are then used to relate test observations to the proposed nonisotropic model. Following a review of coordinate system definitions and transformations used to calculate geometry-dependent parameters in the nonisotropic dispersion model, the procedure for calculating the MBV is presented. This section concludes with a discussion of the nonisotropic microdebris dispersion model and a review of potential nonisotropic distribution functions. The next section applies these methods to microdebris test data to ascertain the validity of the proposed nonisotropic microdebris dispersion model.

Coordinate System Definition

Two coordinate systems are used to simplify the MBV calculations. The first coordinate system is located on the target, with its origin at the target nose. The Z axis goes through the centerline of the target. The X, Y, and Z axes are mutually orthogonal and follow the right-hand rule. If the target has no pitch or yaw, the X axis points up. A schematic of this target coordinate system is shown in Fig. 4. When target pitch or yaw are present, this coordinate system is pitched or yawed with the target. Positive pitch is defined as nose up, that is, clockwise looking down the Y axis. Positive yaw is defined as counterclockwise looking down the X axis. This coordinate system simplifies MBV calculations because the equation of the target surface, that is, a cone, is given by

$$Z^2/L^2 = (X^2 + Y^2)/D^2 \tag{3}$$

The second coordinate system is a fixed test chamber coordinate system, which is used as a reference to relate witness panel locations and MBV calculations. In this coordinate system, rectangular and spherical coordinates are both used. Vectorial calculations are carried out using rectangular coordinates, where Z'' is along the shotline (projectile path) pointing downrange, X'' is pointing up, and Y'' points to the right when looking downrange. The X'', Y'', and Z'' axes are mutually orthogonal and follow the right-hand rule. Double prime notation is used in this coordinate system to reduce confusion between it and the target coordinate system. Figure 5 shows a schematic of this rectangular coordinate system in a test chamber. Dispersion directional calculations are usually performed using spherical coordinates, where angles are measured relative to the Z'' axis. Positive θ is counterclockwise when viewed from above, and positive ϕ is up. Transformations between these coordinate systems are discussed in the next subsection.

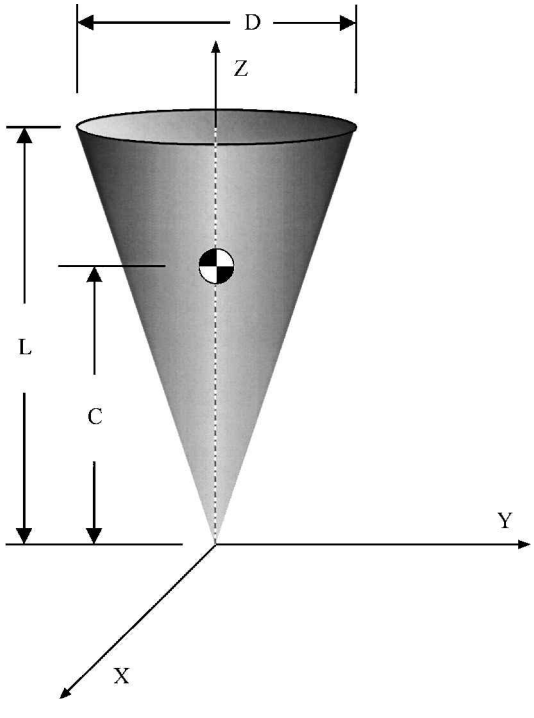

Fig. 4 Target coordinates.

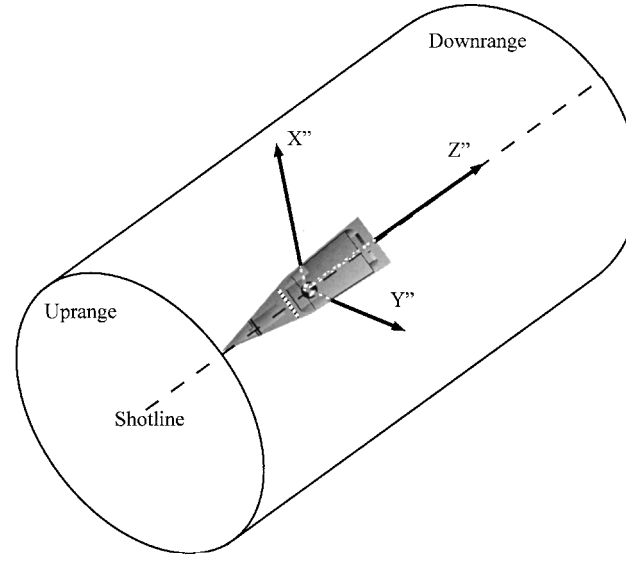

Fig. 5 Rectangular chamber coordinates.

Coordinate System Transformations

Target to Rectangular Chamber Coordinate Conversion

The target to rectangular chamber coordinate system conversion is used to convert points on the target, that is, target c.g. location and points on the MBV, to have the same frame of reference as witness panel locations. This conversion is performed in two steps. The first step rotates about the X axis, opposite the amount of yaw. The second step rotates about the Y axis, opposite the amount of pitch. Note that both coordinate systems are the same when there is no target pitch or yaw and that no conversion is necessary.

The first conversion is about the target X axis. A temporary target coordinate system is used in this development, and parameters in this temporary coordinate system are denoted using a prime notation. Because this is a rotation about the X axis, the X' axis and coordinates remain unchanged. An arbitrary point P, with coordinates X_p, Y_p, and Z_p on the target, is transformed in this example using Eqs. (4–7). Equation (7) calculates a line segment length from the origin to point P. The angle from this line segment to the positive Y axis is calculated using Eq. (6). Next, the angle from the line segment joining point P and the origin to the new Y' axis is calculated using Eq. (5). The intermediate yaw rotated X', Y', and Z' coordinates for point P are then calculated using

$$X'_p = X_p \tag{4a}$$

$$Y'_p = r_p \cos\delta \tag{4b}$$

$$Z'_p = r_p \sin\delta \tag{4c}$$

where

$$\delta = \beta + \text{yaw angle} \tag{5}$$

$$\beta = \tan^{-1}(Z_p/Y_p) \tag{6}$$

$$r_p = \sqrt{Y_p^2 + Z_p^2} \tag{7}$$

The second conversion is a rotation about the Y' axis, opposite target pitch. Temporary target coordinates are again denoted using a prime. The coordinates of point P' generated in the first conversion are used for the calculations in this rotation. Because this rotation is about the Y' axis, the Y'' axis and coordinates remain unchanged. Equations (8–11) are used in the same manner as Eqs. (4–7) to calculate X'', Y'', and Z'' values in the rectangular chamber coordinate system:

$$X''_p = r'_p \sin\delta \tag{8a}$$

$$Y''_p = Y_p \tag{8b}$$

$$Z''_p = r'_p \cos\delta \tag{8c}$$

where

$$\delta' = \beta' - \text{pitch angle} \tag{9}$$

$$\beta' = \tan^{-1}(X'_p/Z'_p) \tag{10}$$

$$r'_p = \sqrt{X'^2_p + Z'^2_p} \tag{11}$$

Rectangular to Spherical Chamber Coordinate Conversion

The rectangular to spherical test chamber coordinate system transformation is performed for generic point P, using Eqs. (12–16). Equation (12) calculates range. Equations (13) and (14) calculate the horizontal angle θ_p (in degrees) from the Z'' axis for Y''_p values greater than and less than zero, respectively. The vertical angle ϕ_p is calculated using Eqs. (15) and (16) for X''_p values less than and greater than zero, respectively:

$$R_p = \sqrt{X''^2_p + Y''^2_p + Z''^2_p} \tag{12}$$

$$\theta_p = \tan^{-1}\left(\frac{Z''_p}{Y''_p}\right) - 90 \quad \text{for} \quad Y''_p > 0 \tag{13}$$

$$\theta_p = \tan^{-1}\left(\frac{Z''_p}{Y''_p}\right) + 90 \quad \text{for} \quad Y''_p < 0 \tag{14}$$

$$\phi_p = \cos^{-1}\left[\frac{Y''^2_p + Z''^2_p}{\sqrt{Y''^2_p + Z''^2_p}\sqrt{X''^2_p + Y''^2_p + Z''^2_p}}\right] \quad \text{for} \quad X''_p < 0 \tag{15}$$

$$\phi_p = -\cos^{-1}\left[\frac{Y''^2_p + Z''^2_p}{\sqrt{Y''^2_p + Z''^2_p}\sqrt{X''^2_p + Y''^2_p + Z''^2_p}}\right] \quad \text{for} \quad X''_p > 0 \tag{16}$$

Spherical to Rectangular Chamber Coordinate Conversion

The spherical to rectangular test chamber coordinate system transformation is performed for generic point P, using Eqs. (17a–17c). These equations calculate the X''_p, Y''_p, and Z''_p values, respectively,

$$X''_p = R_p \sin\phi_p \tag{17a}$$

$$Y''_p = -R_p \cos\phi_p \sin\theta_p \tag{17b}$$

$$Z''_p = R_p \cos\phi_p \cos\theta_p \tag{17c}$$

MBV Calculation

The MBV is calculated using several target and impact geometry parameters, including target length, diameter, pitch, yaw, and position relative to the projectile path in the impact chamber. The MBV is used to provide a reference direction pointing from the target c.g. through a point on the target surface where the projectile first makes contact with the target. Visual test observations, for example, velocimeter disks, soft-catch material damage, etc., indicate shielding by large undamaged target debris is taking place during an impact, which reduces the amount of microdebris dispersed in directions opposite the MBV. Microdebris deposition on witness panel locations relative to the MBV is used as the basis for development of the nonisotropic dispersion model, which is discussed in the following sections.

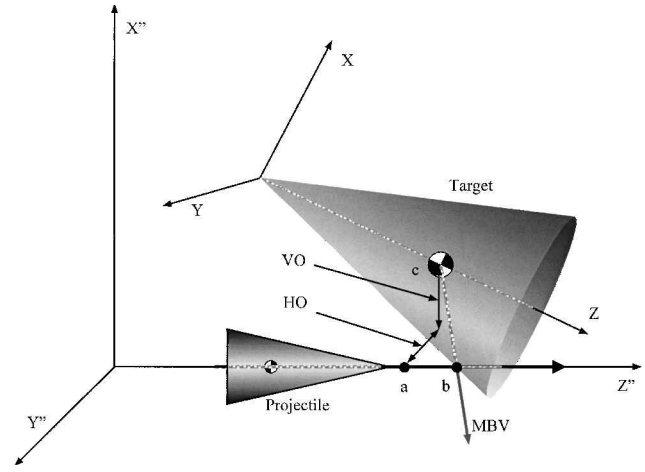

Fig. 6 MBV geometry.

Calculation of the MBV is performed in a series of steps. Figure 6 shows a generic impact scenario, where the projectile impacts the aft target area at point b, which is always on the target surface. Point c is the target c.g. location, whereas point a is located along the shotline (or projectile path) at a vertical offset (VO) and horizontal offset (HO) distance from point c (in the chamber coordinate system). Points b and c are used to define the MBV. VO is parallel to the X'' axis and HO is parallel to the Y'' axis. Depending on the amount of VO and HO for any given test geometry, point a may be inside or outside the target. The target (and target coordinate system) is rotated about its c.g. by the amount of pitch and yaw on each test. Positive pitch and yaw are target nose rotations in the positive X and Y axis directions, respectively. A vector passing through point b with its origin at point c defines the MBV.

The target coordinate system is used to solve a system of equations for point b, that is, X_b, Y_b, and Z_b, on the surface of the target. Equation (3) gives the mathematical equation for the surface of a cone in terms of target geometry shown in Fig. 5. A set of symmetric equations for a line representing the projectiles path (or shotline) through the target surface in the target coordinate system is then substituted into Eq. (3) and solved for X_b, Y_b, and Z_b.

Figure 7 shows a two-dimensional view in the Y–Z (yaw) plane to demonstrate relationships used in this plane to generate these symmetric equations. Nearly identical relationships apply in the X–Z (pitch) plane. Coordinates for point c are given as follows:

$$X_c = 0.0 \tag{18a}$$

$$Y_c = 0.0 \tag{18b}$$

$$Z_c = C \tag{18c}$$

Coordinates for point a are calculated from the impact geometry and are given as follows:

$$X_a = \text{VO}\cos(\text{pitch angle}) \tag{19a}$$

$$Y_a = \text{HO}\cos(\text{yaw angle}) \tag{19b}$$

$$Z_a = C - \text{HO}\sin(\text{yaw angle}) - \text{VO}\sin(\text{pitch angle}) \tag{19c}$$

where the yaw and pitch angles are defined in Fig. 7. The solid triangle with corners at points a and c in Fig. 7 is used to generate Eq. (19b) and the first two terms in Eq. (19c). Similar relationships

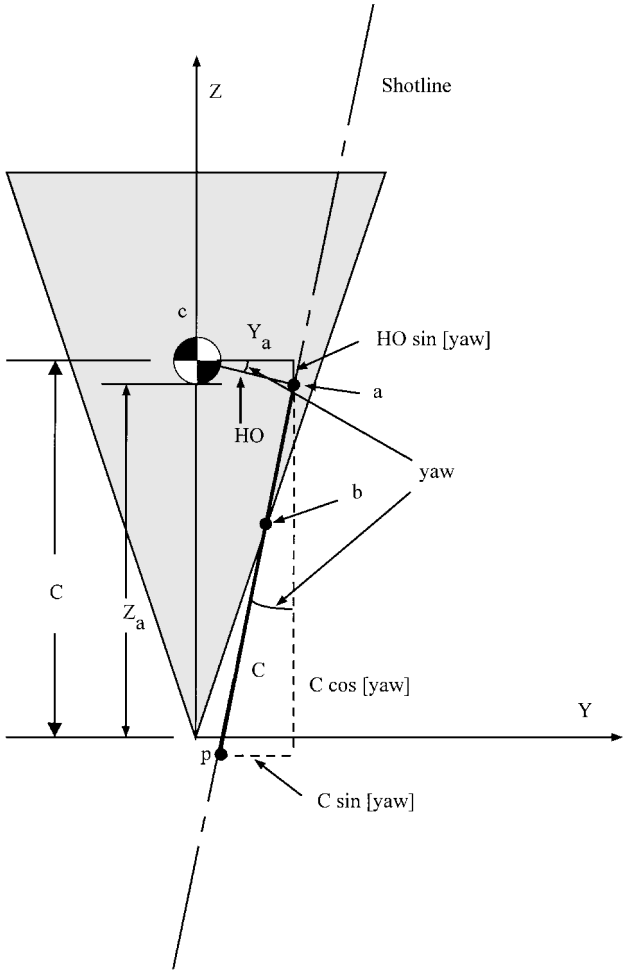

Fig. 7 *X–Y* plane geometry.

in the pitch plane are used to generate Eq. (19a) and the last term in Eq. (19c).

Next, another point on the shotline is needed to complete the symmetric equations. This temporary point p is shown in Fig. 7. Line segment ***ap*** has length C to simplify the symmetric equations. Coordinates for point p are given as follows:

$$X_p = X_a - C\sin(\text{pitch angle}) \tag{20a}$$

$$Y_p = Y_a - C\sin(\text{yaw angle}) \tag{20b}$$

$$Z_p = Z_a - C\cos(\text{yaw angle}) + Z_a - C\cos(\text{pitch angle}) \tag{20c}$$

The dashed line triangle in Fig. 7 is used to generate Eq. (20b) and the first two terms in Eq. (20c). Similar relationships in the pitch plane are used to generate Eq. (20a) and the last two terms in Eq. (20c).

Now that target coordinates of two points on line segment ***ap*** are known, they are substituted into the symmetric equations for a line as given by Eq. (20c). Expressions for the coordinates defining points a and p as given by Eqs. (19a–19c) and (20a–20c) are substituted into

$$(X - X_a)/(X_p - X_a) = (Y - Y_a)/(Y_p - Y_a) = (Z - Z_a)/(Z_p - Z_a) \tag{21}$$

to obtain expressions for X and Y in terms of Z. Next these expressions are substituted into Eq. (3) and solved for Z, which is the Z coordinate for point b, Z_b, in the target coordinate system. The X and Y coordinates for point b, X_b and Y_b, are calculated by substituting $Z = Z_b$ into Eq. (21) and solving for X and Y. The last step is to convert the MBV from target coordinates to the chamber coordinate system. Points b and c, which define the MBV, are simply converted to target coordinates using Eqs. (4–11).

Model Concept and Geometry Definition of Nonisotropic Microdebris Cloud Model

As already mentioned, test data indicate that more microdebris is dispersed in directions not shrouded by large target debris following an impact, whereas the current KIDD model assumes isotropic microdebris dispersion. A method that uses the impact geometry-dependent MBV developed previously is now presented in an attempt to improve the KIDD microdebris dispersion direction model. This is accomplished using a distribution function that predicts microdebris dispersion directions relative to the MBV. A new elevation angle parameter α is used to define dispersion angle relative to the MBV. Figure 8 shows an example of this geometry. An imaginary sphere with radius r is shown in Fig. 8 to assist in visualizing the three-dimensional geometry of this model. The MBV is calculated with points b and c using pretest target geometry and impact conditions. The posttest MBV passes through this imaginary sphere at point m in Fig. 8 and moves with the posttest debris cloud center of mass after impact. The posttest target center of mass is assumed stationary for tests used in these analyses because the expansion velocity is much greater than the target debris cloud center of mass.[4]

Values for α range from 0 to 180 deg, with a value of 0 deg indicating a dispersion elevation angle in the direction of the MBV, whereas a value of 180 deg indicates a dispersion elevation angle opposite the MBV. At constant elevation angles, isotropy is assumed at all azimuth angles. For example, points q, s, and t in Fig. 8 have the same elevation angle relative to the MBV and receive the same predicted microdebris environment.

Several different functional forms of the elevation angle α were evaluated for suitability of use in subsequent analyses. The functional form ultimately selected is based on the beta probability distribution function. This form was chosen because, like α, the beta distribution has discrete maximum and minimum values. These discrete values will ensure that elevation angles less than 0 or greater than 180 deg are not selected. The beta probability density for an interval $0 < \alpha < 180$ deg is given as

$$f(\alpha) = \frac{\Gamma(\lambda+\gamma)}{\Gamma(\lambda)\Gamma(\gamma)}\left(\frac{\alpha}{180}\right)^{\lambda-1}\left(1-\frac{\alpha}{180}\right)^{\gamma-1}\Big/180 \tag{22}$$

where $f(\alpha)$ is the probability density for λ and γ values greater than zero.

In the next section, comparisons of empirically observed dispersion directions relative to the MBV are used to correlate beta function λ and γ parameters in an attempt to model the observed nonisotropic dispersion directions. This form of the distribution function will be shown to possess the characteristics necessary to represent

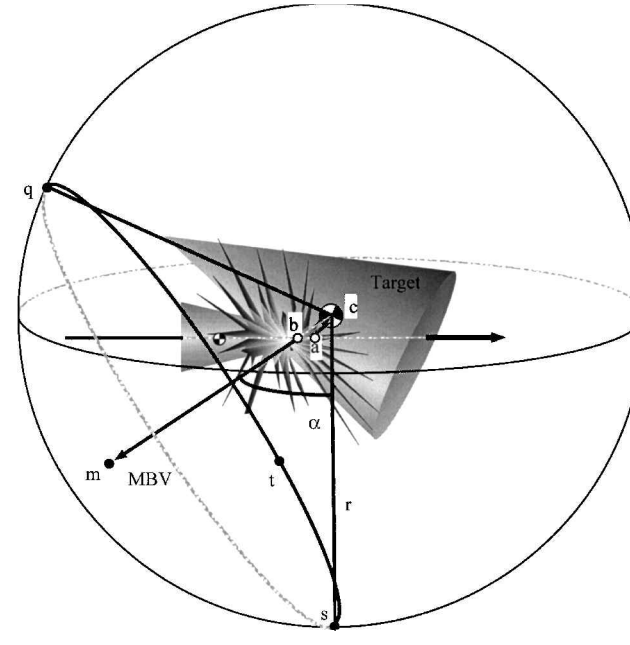

Fig. 8 Small elevation angle example.

correctly the trends observed in the limited test data available and in numerous photographs taken 1 ms after impact.

Model Comparison with Test Data

Introductory Comments

Sapphire witness panel test data are used to evaluate the nonisotropic microdebris dispersion model proposed in the preceding section.[4] Comparisons between measured test data and the predictions of the isotropic KIDD model, especially the distribution slope for small particles, are addressed as well. The normalization techniques discussed earlier are used to ensure all comparisons are surface area normalized based on a 150-cm spherical radius. An additional normalization method is also developed to allow data from multiple tests, with different MBV directions and microdebris environments, to be combined.

In this section, the method used to calculate elevation angle, which is used to relate the impact point to the witness panel location on each test, is presented and discussed. The method used to calculate deposition ratios, which are defined as the ratio of measured microdebris deposition on a witness panel to the number of microdebris fragments predicted using the isotropic KIDD model, is also presented. The deposition ratio also allows data from different tests with varying impact geometries and large fragment size distributions to be combined using KIDD predictions as a baseline.

Elevation Angle Calculation

All witness panel locations are identified in terms of their elevation angle α relative to the MBV. Impact geometry and witness panel locations are used, on each test, to calculate vectors from the target to the MBV and witness panel coordinates in the chamber coordinate system, respectively. A dot product is then used to calculate α for each witness panel as follows:

$$\alpha = \cos^{-1}\left(\frac{\mathbf{MBV}\cdot \boldsymbol{cp}}{\|\mathbf{MBV}\|\,\|\boldsymbol{cp}\|}\right) \tag{23}$$

where the **MBV** is calculated using points c and b as defined in Fig. 6, and $\boldsymbol{cp}$ is the vector between point c (the target c.g.) and point p, which represents the location of a witness panel. These calculated values of α are used for comparisons between depositions observed on each witness panel and distribution function predictions at those angles.

Deposition Ratio Calculation

Microdebris witness panel test data for the various tests are combined by normalizing measured size distributions with respect to isotropic KIDD predictions for each test. This is necessary because the different impact geometries for each test result in debris distributions of different magnitudes. Normalization is performed by calculating the deposition ratio, which is the ratio of the measured size distribution number of fragments per square centimeter at 10 μm to the isotropic KIDD prediction at 10 μm. Because measured fragment sizes calculated from test data are subject to growth factor related uncertainties, the deposition ratios are also obtained assuming 3× and 5× growth factors.

Test Data Comparison with Existing KIDD Model

Figure 9 shows calculated witness panel deposition ratios using the original isotropic KIDD baseline. The open symbols in Fig. 9 represent data where no evidence of projectile microdebris was found with the SEM/EDX, that is, target deposition only. The diamond symbols represent data where projectile microdebris deposition in addition to target microdebris was observed. Measured microdebris size distributions from these samples, therefore, are greater than deposition containing only target microdebris and are not considered to be relevant data for development of the nonisotropic dispersion model. The error bar magnitudes in Fig. 9 represent 5× growth factor deposition ratio values.

The comparison in Fig. 9 indicates KIDD may be underpredicting the amount of microdebris at nearly all elevation angles from the MBV by an order of magnitude or more. One way of improving the accuracy of the KIDD predictions is by increasing the KIDD size distribution slope. This slope cannot be increased too much, however, because fragment mass will not be conserved without substantial changes to the large fragment size distribution. The next subsection summarizes the results of modified KIDD runs with increased size distribution slopes that were performed to reduce differences between KIDD and measured test data. Nonisotropic dispersion angle distribution functions are then compared to test data using these modified KIDD size distributions.

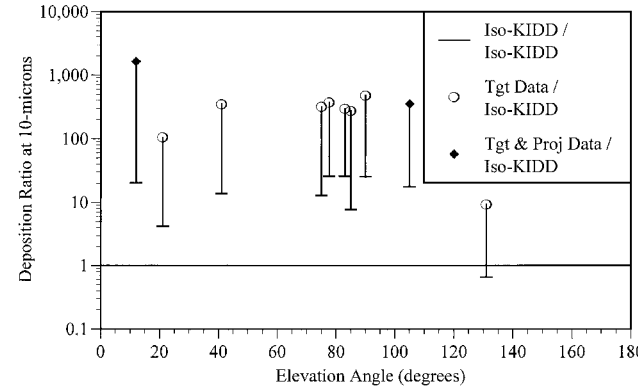

Fig. 9 Deposition ratio comparison.

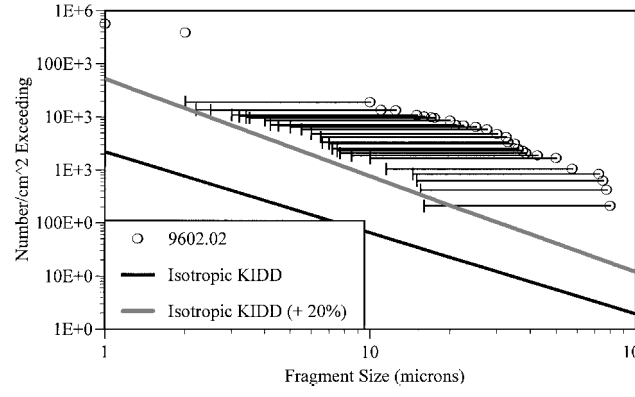

Fig. 10 KIDD 20% slope increase size distribution for sample 9602.02.

KIDD Size Distribution Slope Adjustments

A series of KIDD runs were made with modified size distribution slopes to investigate sensitivities between slope and the amount of microdebris. As already mentioned, the integral of the entire fragment size distribution gives the mass sum of all fragments, which must equal the preimpact target mass. Care must be used, therefore, to ensure that an increase in size distribution slope at micrometer sizes does not significantly change the size distribution at large fragment sizes.

Modified KIDD runs were made with size distribution slope increases of 10, 20, and 30%. Runs with a 10% slope increase only yielded a slight increase in the predicted amount of microdebris. Runs with a 30% or more increase in size distribution slope resulted in significant and unacceptable changes in the large fragment distributions. These changes were a direct result of mass conservation enforcement because the number of large fragments was reduced to account for the increased number and, therefore, mass of smaller fragments.

Size distribution slope increases of 20% resulted in the greatest increase in predicted microdebris without significantly changing large fragment distributions. Therefore, it was decided to limit the slope increase to 20% and use it to replot the comparison shown as an example in Fig. 3. Figure 10 shows microdebris size distributions from the 20% slope increase KIDD runs. Also shown in Fig. 10 are the same measured deposition data with 5× growth factor error bars and nominal isotropic KIDD predictions that were shown in Fig. 3.

Examination of Fig. 10 indicates much closer agreement between the modified isotropic KIDD predictions and the measured test data.

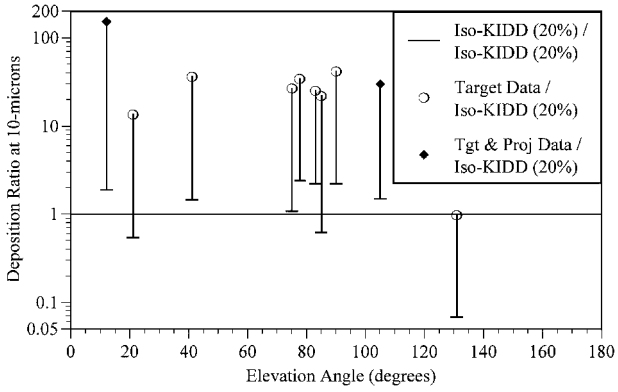

Fig. 11 Deposition ratios for KIDD 20% slope increase.

Figure 11 compares deposition ratios at 10 μm between test data and modified 20% slope increase isotropic KIDD runs for the same witness panels shown in Fig. 9. The baseline isotropic KIDD values in Fig. 11 used to calculate deposition ratios are taken from the increased slope size distributions at 10 μm shown in Fig. 10. We note that in Fig. 10 the proposed nonisotropic KIDD modifications have not yet been implemented. In the next subsection, the effects of implementing these nonisotropic modifications on the agreement between KIDD predictions and test data are explored.

Nonisotropic Distribution Function Parameter Evaluation

The beta distribution function selected earlier and given by Eq. (22) is examined in this section as a potential nonisotropic function to better model the dispersion elevation angle in KIDD. All comparisons between test data and KIDD model predictions in this section will use as a baseline the modified 20% size distribution slope increases as discussed in the preceding section.

Two parameters, λ and γ, govern the shape of the beta distribution function. When $\lambda = 1$ and $\gamma > 1$, the beta function has its maximum value at 0 deg. When $\lambda > 1$ and $\gamma > 1$, the maximum value lies somewhere between 0 and 180 deg. Target microdebris deposition ratio comparisons shown in Figs. 9 and 11 indicate greater amounts of target microdebris was dispersed at elevation angles between 40 and 100 deg. This is consistent with laser photographs taken a few microseconds after impact. Figure 12 shows a laser photograph from a light-gas gun test. In this test, the camera is forward and off to the side from the hanging target. The projectile enters from the right. In this test, the MBV points in an uprange direction, that is, to the right. Microdebris is observed in Fig. 12 as expanding in the shape of an annulus about the impact point. There is downrange shrouding by the target and uprange shrouding by the projectile; thus most microdebris is directed to elevation angles between 40 and 100 deg from the MBV. As will be seen shortly, a beta distribution function adequately models this type of phenomenon.

Because we have only a limited amount of witness panel data from any single test, a quantitative statistical curve-fitting analysis to determine the optimum values of λ and γ does not appear to be an appropriate exercise at this time. Qualitative analyses will, therefore, be performed on the combined target microdebris test data discussed in the last section so that appropriate beta distribution function parameters are obtained. Table 1 shows the sets of λ and γ values to be used in comparisons between nonisotropic beta dispersion direction distribution function predictions and test data. Function D is the most conservative and represents nonisotropic dispersion that is spread out over a large number of elevation angles. It predicts more microdebris dispersion than the isotropic model at elevation angles between 25 and 115 deg.

Function C in Table 1 has a peak value at an elevation angle of 70 deg, which is four times larger than an isotropic function. It predicts more microdebris dispersion than the isotropic model at elevation angles between 45 and 105 deg, but very little dispersion at elevation angles smaller than 30 deg and larger than 125 deg. Function E is the most nonisotropic of the three shown in Table 1. It has a peak value 7.5 times larger than an isotropic function at an elevation angle of 80 deg and predicts more microdebris dispersion

Table 1 Beta distribution function parameters

Distribution function	λ	γ
C	10.0	14.0
D	3.0	4.5
E	40.0	50.0

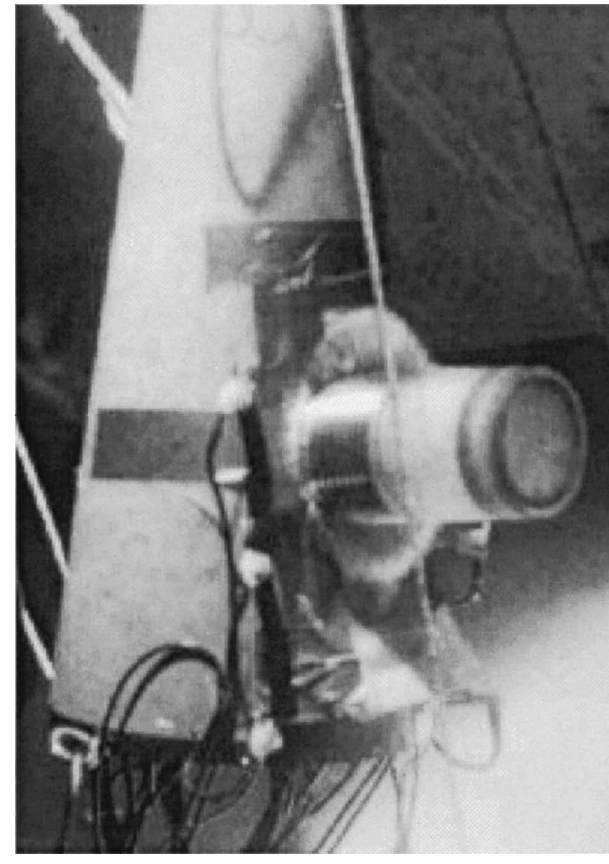

Fig. 12 Postimpact laser photograph.

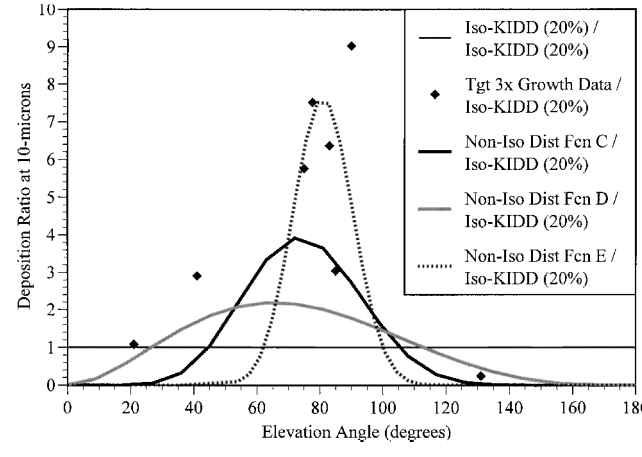

Fig. 13 Nonisotropic distribution function for 3× growth factor test data.

than the isotropic model at elevation angles between 62 and 100 deg. However, this function predicts very little dispersion at elevation angles smaller than 55 deg and larger than 110 deg.

Figures 13 and 14 show a comparison between 3× and 5× growth factor target debris deposition ratio data, respectively, and deposition ratios for the three beta distribution functions described in Table 1. Both the test data and beta distribution functions use the modified isotropic 20% size distribution slope increase KIDD predictions as a baseline, shown in Figs. 13 and 14 as the horizontal line with a deposition ratio of one. The microdebris data in Figs. 13 and 14 are

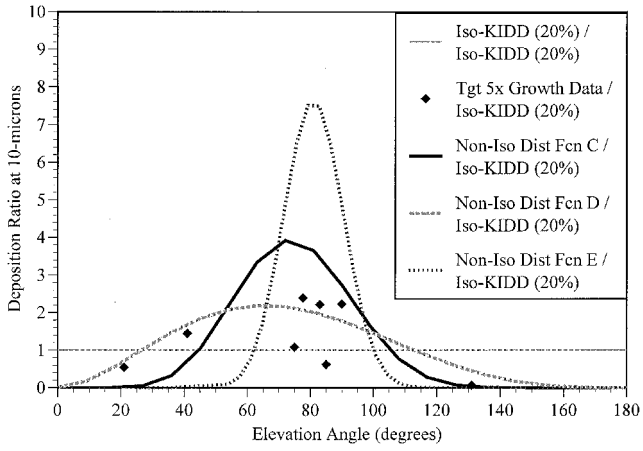

Fig. 14 Nonisotropic distribution function for 5× growth factor test data.

for witness panel elevation angles relative to the MBV. We note that the MBV is unique to each test impact and target geometry and does not always point in the same direction in every test.

In Fig. 13, nonisotropic dispersion direction distribution function *C* appears to be the best match to the data shown. It underpredicts the amount of measured 3× growth factor microdebris by roughly the same amount at most elevation angles. It does, however, reflect the greater amount of microdebris test data observed at elevation angles between 70 and 80 deg. Distribution function *D* is rejected in this comparison because it does not have a large enough peak at 80 deg. Distribution function *E* is rejected in this comparison because it does not predict enough microdebris at elevation angles smaller than 40 deg. It does, however, have a desirable large peak near 80 deg. Unfortunately, both a large peak and wide dispersion pattern cannot be modeled in the same function because the area under the curve must equal the area under the isotropic KIDD baseline. Figure 14 uses the same linear *y*-axis and upper *y*-axis value as Fig. 13 to simplify relative magnitude comparisons between 3× data, 5× data, and the nonisotropic distribution functions in Figs. 13 and 14. Nonisotropic dispersion direction distribution function *D* appears to be the best match to the 5× growth factor data in Fig. 14.

Considerable scatter in test data is observed in Figs. 13 and 14 at elevation angles between 70 and 90 deg. This scatter results because multiple impact geometry and target damage levels are possible. The data in Figs. 13 and 14 are ratios of actual depositions to KIDD predictions for different tests. Because some impacts are not as catastrophic as others and because KIDD cannot make perfect predictions for every level of damage, some scatter in the plots is to be expected. The three points with the largest deposition ratio values in this region are representative of the majority of impact geometries for which KIDD is intended to be used. Therefore, when the beta distribution functions were compared in Figs. 13 and 14, agreement with the larger values in this range was a higher priority.

More test data are needed at all elevation angles and impact geometries to generate upper and lower bounds for this scatter. The fact that distribution function *C* is a better match to the 3× growth factor test data and distribution function *D* is a better match to the 5× growth factor test data highlights the importance of the need to gain a better understanding of growth factor phenomena. However, these results do show that a beta distribution function model for elevation angle is capable of matching empirical data, although clearly additional data are needed for further validation and confirmation.

Conclusions

There exists a need to be able to quantify accurately the microdebris environments associated with hypervelocity impacts of complex targets. We have used available microdebris data to develop a nonisotropic dispersion model that can be used to characterize these environments. Comparisons of model predictions with experimental results revealed strengths and weaknesses in the model, but, more important, identified what type of test data are needed to continue this research. Specifically, additional microdebris impact tests would have to be performed to allow the collection of microdebris data at many different elevation angles and impact geometries. Data at all elevation angles cannot be collected, however, because some angles will be in the projectile debris cloud. Dedicated microdebris experiments using a particle accelerator are also needed to reduce growth factor uncertainties. These types of efforts should also generate sufficient data to select the best nonisotropic elevation angle distribution function.

Acknowledgments

Special thanks are extended to Kevin Nash of the Theater High Altitude Area Defense Project Office and David Mayo of the U.S. Army Space and Missile Defense Command for supporting the research described in this paper. The authors also express sincere gratitude to Walter R. Mendes, William Sommers, and Robert Varnon for their valuable time and efforts in helping to complete this work.

References

[1]Sommers, W. J., Kruse, G. R., and Weed, R. A., "KIDD Kernel Version 3.5," Nichols Research Corp., Rept. NRC-N-TR-98-099, Huntsville, AL, 1998.

[2]Sommers, W. J., Kruse, G. R., Weed, R. A., and Mayo, D. V., "Radar Cross Sections and Ballistic Coefficients of Fragments from Impacts with Complex Full-Scale Targets," *International Journal of Impact Engineering*, Vol. 20, Nos. 1–4, 1997, pp. 753–764.

[3]Sommers, W. J., Kruse, G. R., Johnston, J. W., Atha, L. C., and Henderson, J. C., "Spin Velocimeters for Impact Debris Fragments," *International Journal of Impact Engineering*, Vol. 17, Nos. 1–4, 1995, pp. 773–784.

[4]Kruse, G. R., Mendes, W. R., Sommers, W. J., Weed, R. A., Nash, K. D., and Mayo, D. V., "Testing and Simulation of Microdebris from Impacts with Complex Targets," *International Journal of Impact Engineering*, Vol. 23, Nos. 1–4, 1999, pp. 489–500.

E. R. Johnson
Associate Editor